Progress In Electromagnetics Research M, Vol. 102, 137–148, 2021

Transverse-EPT: A Local First Order Electrical Properties Tomography Approach Not Requiring Estimation of the Incident Fields

Reijer Leijsen[1, *], Wyger Brink[1], Xin An[2], Andrew Webb[1], and Rob Remis[2]

Abstract—A new local method for magnetic resonance electrical properties tomography (EPT), dubbed transverse-EPT (T-EPT), is introduced. This approach iteratively optimizes the dielectric properties (conductivity and permittivity) and the z-component of the electric field strength, exploiting the locally E-polarized field structure typically present in the midplane of a birdcage radiofrequency (RF) coil. In contrast to conventional Helmholtz-based EPT, T-EPT does not impose homogeneity assumptions on the object and requires only first order differentiation operators, which makes the method more accurate near tissue boundaries and more noise robust. Additionally, in contrast to integral equation-based approaches, estimation of the incident fields is not required. The EPT approach is derived from Maxwell's equations and evaluated on simulated data of a realistic tuned RF coil model to demonstrate its potential.

1. INTRODUCTION

In electrical properties tomography (EPT), the goal is to obtain quantitative conductivity (σ) and, to a lesser extent, permittivity (ε) maps from non-invasive measurements of the circularly polarized radiofrequency transmit field $B_1^+ = (B_x + \mathrm{j}B_y)/2$ acquired with a magnetic resonance scanner. Since the conductivity influences the specific absorption rate (SAR), EPT has potential applications in hyperthermia treatment planning and SAR assessment [1, 2]. Additionally, due to the relation between ionic content and tissue conductivity, conductivity may provide a useful biomarker in tumour diagnostics [3, 4]. A large number of EPT methods are currently available [5–7]; however, they all suffer from one or multiple challenges such as noise sensitivity, the need for estimation of the incident electromagnetic fields, or a high computational demand.

Here, we present a new approach, dubbed transverse-EPT (T-EPT), which exploits the E-polarized field structure typically present in the midplane of a birdcage radiofrequency (RF) coil [8], an assumption that is frequently used for two-dimensional EPT approaches [9, 10]. In contrast to conventional Helmholtz-based EPT (H-EPT) [11, 12], this approach does not impose assumptions on the spatial homogeneity of the tissue structures, which would otherwise degrade reconstructions around tissue interfaces and small tissue structures. Additionally, the proposed method involves only first order differentiation operators acting on B_1^+ instead of second or higher order derivatives, improving noise robustness [11, 13]. Furthermore, in contrast to integral-based methods, this method does not require knowledge of incident fields, making the method easier to apply [9, 10] and, in contrast to data-based methods, no training data is required to allow for generalization [14, 15]. Finally, compared to three-dimensional methods that take all field components into account [16–18], this technique is fast and easy to implement.

Received 10 February 2021, Accepted 26 April 2021, Scheduled 11 May 2021
* Corresponding author: Reijer Leijsen (R.L.Leijsen@lumc.nl).
[1] C.J. Gorter Center, Leiden University Medical Center, The Netherlands. [2] Circuits and Systems Group, Delft University of Technology, The Netherlands.

Through Maxwell's equations, we derive the two fundamental equations that relate the B_1^+ field to the electrical properties (EPs) and z-component of the electric field strength (E_z). These two equations are then combined in an objective function, which is minimized to estimate the EPs. Numerical experiments on both a head and pelvis model are performed in two- and three-dimensional configurations with a realistic RF coil model to evaluate the effect of field components that are not accounted for in the E-polarized field representation. Moreover, the effects of the transceive phase assumption (TPA) [19] as well as noise are evaluated to show the potential of T-EPT.

2. THEORY

The fundamental assumption of T-EPT is that longitudinal variations of the longitudinal magnetic field and transverse electric field can be neglected within the midplane of a birdcage coil. A purely E-polarized electromagnetic field satisfies this assumption, and we therefore consider the z-component of the Maxwell-Ampère law and the x- and y-components of Faraday's law to arrive at the fundamental EPT equations. Specifically, in steady state (time factor $\exp(\mathrm{j}\omega t)$) the z-component of the Maxwell-Ampère's law is given by

$$\partial_y B_x - \partial_x B_y + \mu_0 \eta E_z = 0 \tag{1}$$

with μ_0 the permeability of free space (air) and $\eta = \sigma + \mathrm{j}\omega\varepsilon$ the admittance containing the EPs (σ and ε). Now in EPT, the B_1^+ field is considered known through measurements and the above Maxwell equation can be used to relate this measured field to ηE_z, the z-component of the induced electric current density. In particular, by acting with the Wirtinger derivative $\partial^- = (\partial_x - \mathrm{j}\partial_y)/2$ on the B_1^+ field, we obtain

$$\begin{aligned}
\partial^- B_1^+ &= \frac{1}{4}\left[\partial_x B_x + \partial_y B_y - \mathrm{j}\left(\partial_y B_x - \partial_x B_y\right)\right], \\
&= \frac{1}{4}\left(\partial_x B_x + \partial_y B_y + \mathrm{j}\mu_0 \eta E_z\right), \\
&= \frac{1}{4}\left(-\partial_z B_z + \mathrm{j}\mu_0 \eta E_z\right),
\end{aligned} \tag{2}$$

where we used Equation (1) in the first step and Gauss' law of magnetism ($\partial_x B_x + \partial_y B_y + \partial_z B_z = 0$) in the second step. For relatively large human tissue structures in the midplane of a birdcage RF coil we typically have $|\partial_z B_z| \ll |\mu_0 \eta E_z|$ which allows for setting $\partial_z B_z \approx 0$, which is consistent with our assumption on the structure of the electromagnetic field, and the previous equation can therefore be simplified to

$$\frac{4}{\mathrm{j}\mu_0}\,\partial^- B_1^+ = \eta E_z, \tag{3}$$

which relates first-order derivatives of the data to the product of η and E_z. This is our first fundamental T-EPT equation.

Subsequently, we consider the x- and y-components of Faraday's law and write these equations as

$$B_x = -\frac{1}{\mathrm{j}\omega}\left(\partial_y E_z - \partial_z E_y\right) \quad \text{and} \quad B_y = \frac{1}{\mathrm{j}\omega}\left(\partial_x E_z - \partial_z E_x\right). \tag{4}$$

Substituting these expressions in the definition of the B_1^+ field gives

$$B_1^+ = \frac{1}{2}(B_x + \mathrm{j}B_y) = \frac{1}{\omega}\left(\partial^+ E_z - \partial_z E^+\right), \tag{5}$$

with $\partial^+ = (\partial_x + \mathrm{j}\partial_y)/2$ and $E^+ = (E_x + \mathrm{j}E_y)/2$. In the neighbourhood of the midplane of a birdcage RF coil we typically have $|\partial_z E^+| \ll |\partial^+ E_z|$ which allows setting $\partial_z E^+ \approx 0$, and therefore in this region the above equation simplifies to

$$B_1^+ = \frac{1}{\omega}\,\partial^+ E_z. \tag{6}$$

This is our second fundamental T-EPT equation. We note that a purely E-polarized field ($E_x = E_y = B_z = 0$) satisfies the two fundamental T-EPT equations (3) and (6) exactly. Also note the dual character

of both equations: a Wirtinger derivative of B_1^+ is proportional to E_z, while a Wirtinger derivative of E_z is proportional to B_1^+.

Having the fundamental T-EPT equations available, we attempt to reconstruct the admittance η, and thus the EPs, by minimizing the discrepancy in Equations (3) and (6). To this end, let $\|\cdot\|$ denote the standard two-norm of scalar complex-valued field quantities defined on the midplane of the birdcage coil. We now reconstruct the admittance from available B_1^+ data by iteratively minimizing the objective function

$$F(E_z,\eta)=\frac{1}{2}\frac{\left|\left|\frac{4}{\mathrm{j}\mu_0}\,\partial^- B_1^+-\eta E_z\right|\right|^2}{\left|\left|\frac{4}{\mathrm{j}\mu_0}\,\partial^- B_1^+\right|\right|^2}+\frac{1}{2}\frac{\left|\left|B_1^+-\frac{1}{\omega}\,\partial^+ E_z\right|\right|^2}{\left|\left|B_1^+\right|\right|^2} \tag{7}$$

for the electric field and admittance in an alternating fashion. Specifically, for a fixed admittance, we first update the electric field E_z via a conjugate gradient update (see Appendix A), followed by a least-squares minimization of Equation (3) to obtain η (note that η is present in the first term on the right-hand side of Equation (7) only, which measures the discrepancy in satisfying Equation (3)). These steps are repeated until convergence or a maximum number of iterations is reached. The conductivity and permittivity maps are finally extracted from the real and imaginary part of the admittance.

3. METHODS

Synthetic data was acquired by simulating a 3 T birdcage body transmit coil driven in quadrature at 128 MHz using XFdtd (XF7.5, Remcom State College, PA, USA). The coil had 16 rungs (leg length 420 mm, leg width 40 mm and endring width 80 mm), a length of 580 mm and a diameter of 704 mm, and was surrounded by an RF shield which was 700 mm in length and 743 mm in diameter. The coil model was tuned with endring and leg capacitors with a capacitance of 26.7 pF and 67 pF, respectively, and driven in quadrature mode by two 50 ohm voltage sources with a +90 degree phase shift. The coil model was loaded by either the Duke or Ella body models from the virtual family [20]. The Duke body model had its pelvis centered in the coil, while the Ella body model was centered around its corpus callosum. The models occupy a domain of 190×150 and 109×87 voxels of $2\times2\,\mathrm{mm}^2$ for the pelvis and head model, respectively. For each object the current density distribution on the loaded coils was acquired to simulate two-dimensional settings using in-house simulation code in MATLAB (version 2019b, The MathWorks, Inc., Natick, MA, USA). The electromagnetic fields were extracted and processed to construct the B_1^+ data with transmit phase φ^+. The coil was also driven in anti-quadrature mode with a -90 degree phase shift between the sources in order to construct the transceive phase $\varphi^\pm$ to evaluate the effect of the TPA (estimating the transmit phase as half the transceive phase [19]). Finally, a noisy dataset was constructed by adding complex Gaussian noise to the last described dataset of both models to achieve a signal-to-noise ratio (SNR) of 100 defined as mean B_1^+ over standard deviation of noise [15].

The reconstruction approach was discretized (see Appendix B) and implemented in MATLAB. First, it was tested in a two-dimensional configuration in which all field data are consistent with the E-polarized field representation. Second, it was tested in a three-dimensional configuration to evaluate the effect of field components that are not represented by the E-polarized field structure. Third, the method was tested on transmit field data with a transceive phase distribution and the effect of the TPA therein was evaluated. Finally, the method was tested on noisy data and compared to H-EPT with a $7\times7\times5$ noise suppression kernel as defined in [19, 21]. The iterative process was initialized by estimating the EP maps with H-EPT and by computing E_z through Equation (3). The iterative process was stopped after 1000 iterations.

4. RESULTS

Figure 1 shows absolute maps of the electric field strength components and different phase maps corresponding to the Duke pelvis model and the Ella head model configurations, to indicate the validity of the E-polarized field assumption as well as the accuracy of the TPA. We observe in the pelvis model that the magnitude of the x- and y-components of the electric field strength are significantly smaller

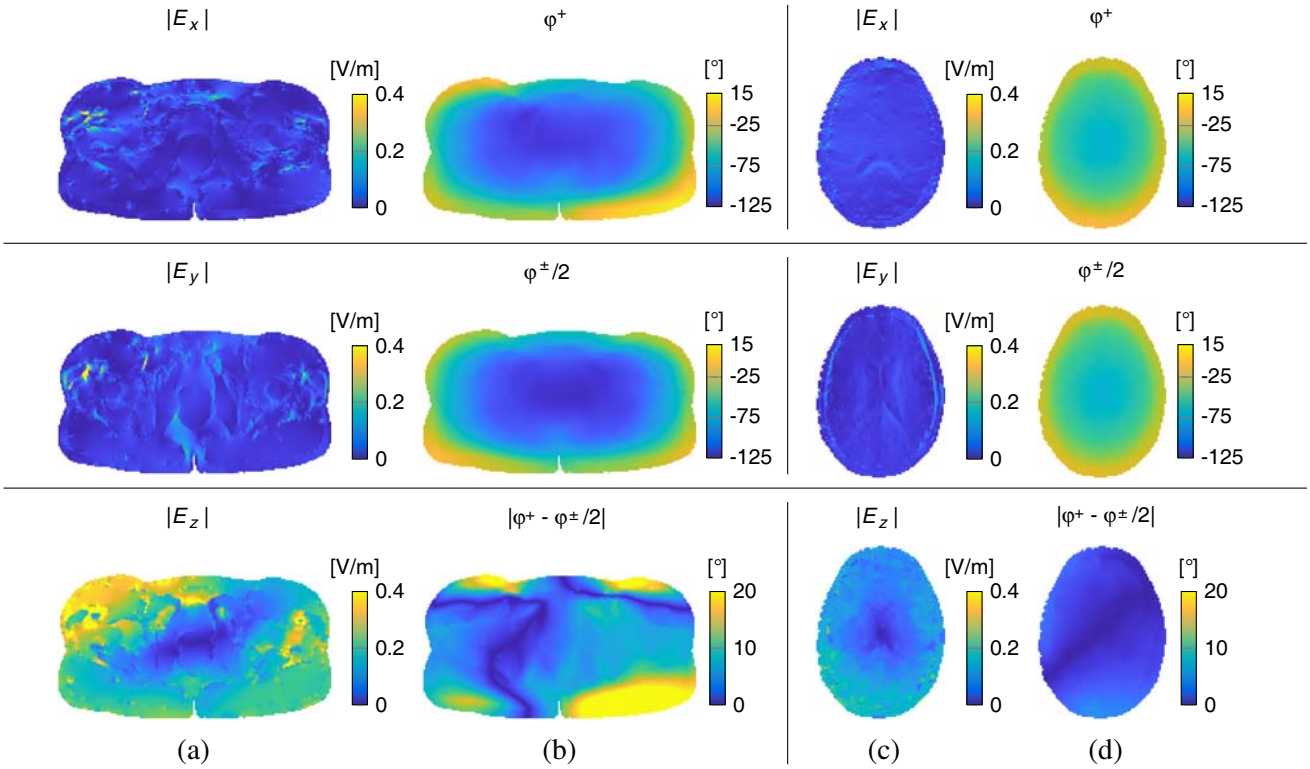

Figure 1. Simulations of the electric field strength and the (absolute difference between) the true transmit field and that estimated from the available transceive phase for (a), (b) the Duke pelvis model and (c), (d) the Ella head model. The magnitude of (a), (c) the electric field strength components and (b), (d) the phase maps.

than the magnitude of the z-component, while this magnitude difference is smaller in the head model configuration. This indicates that the fields conform better to the assumed E-polarized field structure in the pelvis model than in the head model configuration. In contrast, the TPA shows smaller errors in the head model configuration than in the pelvis model configuration, indicating that the TPA is more accurate in the head model than in the pelvis model.

Figure 2 compares the reconstructed conductivities of the Duke pelvis region in the two- and three-dimensional configurations, which are obtained within a few seconds on an Intel i7-6700 CPU with 32 GB memory. (The permittivity results are shown in the supplementary information.) The reconstruction results for a two-dimensional configuration, where the E-polarized field structure is ensured, are shown in Figure 2(b). An artefact is visible on the diagonal of the object which coincides with the region where the magnitude of E_z is low, see Figure 1(a). The result when T-EPT is applied on B_1^+ data with φ^+ generated in a three-dimensional configuration is shown in Figure 2(c). Since the EM field is no longer strictly E-polarized, approximations made to obtain Equations (3) and (6) are not completely satisfied, leading to errors in the reconstructed EPs. The tissue structure is maintained, but larger errors are visible across the diagonal of the object where the magnitude of E_z is small. Finally, Figure 2(d) shows the reconstruction results when the TPA is applied to $\varphi^{\pm}$. The reconstructed conductivity map is different from the map obtained without TPA, but remains of a similar overall quality. Significant differences are mainly observed in the permittivity map, especially at locations where the TPA does not hold.

The conductivity results from the Ella head model are shown in Figure 3. (The permittivity results are shown in the supplementary information.) The reconstructed conductivity map in the two-dimensional configuration has good accuracy in the reconstruction of the tissue structure, but shows large underestimations for high conductivity values, which also coincide with areas of low electric field strength. The three-dimensional configuration shows a larger reconstruction error in the head model

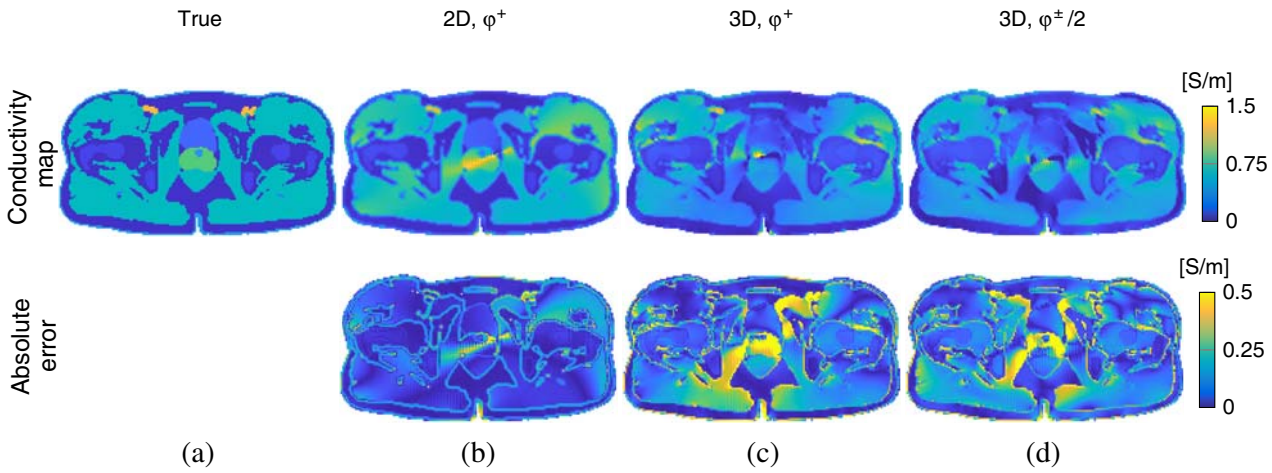

Figure 2. (a)–(d) Reconstructed conductivity and (e)–(h) relative permittivity map, with their corresponding absolute error map, of the Duke pelvis model for different B_1^+ datasets.

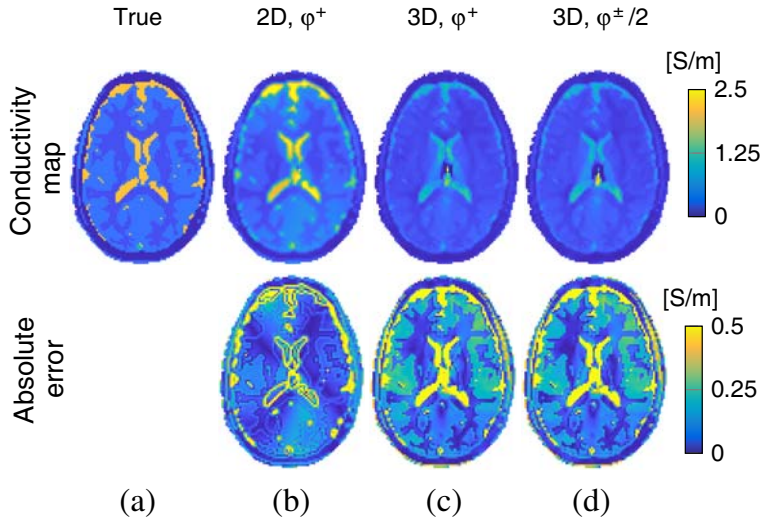

Figure 3. Reconstructed conductivity map (top row) and the corresponding absolute error map (bottom row) of the Ella head model for different B_1^+ datasets.

than in the pelvis model, when compared to their corresponding two-dimensional configurations. This is in agreement with the results observed in Figure 1(c), which shows larger deviations from the E-polarized field structure in the head model when compared to the pelvis model. Figure 3(d) shows the reconstruction when the transmit phase is estimated from $\varphi^{\pm}$ via the TPA, which yields essentially the same reconstruction as when based on φ^{+}. This is in agreement with the results observed in Figure 1(d), which shows relatively small errors due to the TPA.

The T-EPT conductivity reconstruction results of both models with uniform Gaussian noise added to the simulated data are shown in Figure 4 and compared to H-EPT with a noise robust Laplacian kernel. (The permittivity results are shown in the supplementary information.) The first-order differentiation-based T-EPT results are disturbed by the noise, but the underlying tissue structure remains clearly visible. This is in contrast to H-EPT, which utilizes second-order differentiation operators leading to severely degraded reconstructions. The T-EPT reconstruction of the central region with low E_z appears to obtain a similar quality as H-EPT.

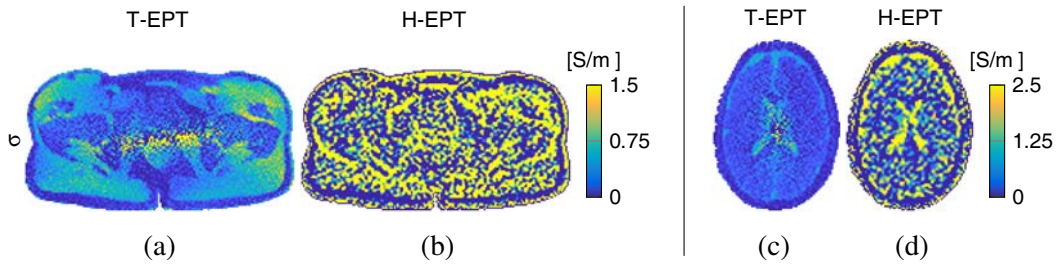

Figure 4. Reconstructed conductivity map of (a), (b) the Duke pelvis model and (c), (d) the Ella head model from noisy three-dimensional transmit field data with an SNR of 100 and with TPA applied.

5. DISCUSSION

T-EPT only applies first-order differences to the data making it significantly more noise robust than H-EPT (which applies second-order differences), even though the H-EPT implementation incorporates noise mitigation strategies while the T-EPT implementation did not. Regularization strategies, such as adding a multiplicative total variation term to the objective function, might further reduce the noise effects on the T-EPT reconstructions [9]. Note that since the proposed approach is fairly straightforward, extensions are relatively easy to implement. Additionally, T-EPT does not require imposing tissue homogeneity assumptions, which are required in Helmholtz-based approaches [11–13, 22], resulting in significantly better reconstruction accuracy at tissue interfaces, allowing also for the reconstruction of smaller tissue structures. Furthermore, the method does not require knowledge of the incident fields, in contrast to integral equation-based EPT approaches [9, 10, 17, 18], making the method easier to apply to and avoiding the need for vendor-specific information on the transmit coil or additional calibration experiments [23]. Also, in contrast to methods based on a dictionary or on machine learning [14, 15], the method does not require an exhaustive set of example data, which can be difficult to obtain. Moreover, the method requires only a few seconds to arrive at a solution, while integral equation-based approaches that take the three-dimensional field structure into account can require several hours [17] up to days [18].

Similar to other two-dimensional approaches in EPT [9, 10], the proposed approach revolves around E_z, and in regions where its magnitude is low, an artefact can be observed. As the conduction and displacement current are low in this region, the underlying EPs leave an inherently weaker imprint on the measured B_1^+ data. These regions can be positioned elsewhere by using a transmit array coil with multiple elements [25], and their effect on the reconstruction can be mitigated by incorporating multiple complementary antenna settings into the objective function [9, 24]. The reconstruction process can be regularized to avoid error-propagation in regions with weak E_z.

In all discussions, we note that the higher accuracy observed in the conductivity maps than the permittivity maps can be assigned to the larger influence of the conduction than the displacement currents on the B_1^+ at this frequency [17]. This finding is in line with many other studies. Although the permittivity results are inaccurate, resulting in essentially meaningless absolute values from a physical point of view, relatively accurate conductivity values can still be obtained.

The 2D reconstructions show that T-EPT is applicable in regions where the longitudinal variations of E_x, E_y, and B_z are small, i.e., in a region where the electromagnetic fields have an E-polarized field structure, which is typically a fair approximation around the midplane of a birdcage coil. However, the results from the 2D and 3D fields indicate a substantial underestimation of the true EP value, indicating that further refinement of the method is warranted. Other anatomical areas where T-EPT may prove useful may include more "cylindrical" body parts such as legs or arms. Additionally, other transmit coil topologies such as TEM coils [26] might satisfy the made assumptions better and may, therefore, provide improved reconstruction performance. We note that numerical experiments of transversal slices several centimeters away from the midplane resulted in EP maps with comparable quality.

The TPA introduces artefacts for non-symmetrical objects [19]. Since the head model is fairly circular and symmetrical, the differences between using φ^+ or $\varphi^{\pm}/2$ are negligible. However, the TPA results in larger reconstruction errors in the pelvis model. Other EPT techniques overcome the unavailability of φ^+ by reformulating the problem in terms of magnitude only [18, 27], in terms of $\varphi^{\pm}$ [28] or in terms of relative phases when a multi-element array is available [29], and these approaches may

also be applicable to T-EPT.

6. CONCLUSION

This manuscript introduces transverse EPT, a new reconstruction technique that is noise robust, accurate at tissue boundaries, fast, easy to implement and does not require knowledge of the incident fields. It builds on the symmetry between the transmit and receive phases typical to magnetic resonance imaging configurations and yields promising reconstruction results in regions where the electromagnetic fields are sufficiently E-polarized, and the z-component of the electric field strength is high. Further validation through simulations and experiments is warranted to further this approach and demonstrate clinical potential.

ACKNOWLEDGMENT

The research was funded by the European Research Council Advanced NOMA MRI under grant number 670629. Thanks to P. S. Fuchs (TU Delft) for fruitful discussions and P. R. S. Stijnman (UMC Utrecht) for the details of the tuned RF coil model.

APPENDIX A. ELECTRIC FIELD UPDATES

After initialization, the z-component of the electric field strength is updated according to the formula

$$E_z^{[n]} = E_z^{[n-1]} + \alpha^{[n]} v^{[n]}, \tag{A1}$$

with α the step length, v the update direction, and n the iteration number. As update direction the Polak-Ribière update directions are taken, which are given by

$$v^{[n]} = g^{[n]} + \frac{\mathrm{Re}\left\langle g^{[n]}, g^{[n]} - g^{[n-1]} \right\rangle}{\left\| g^{[n-1]} \right\|^2} v^{[n-1]}, \tag{A2}$$

where Re denotes the real part, with the inner product and norm restricted to the object domain and defined as in [9]. Furthermore, g is the gradient of the functional from Equation (7) w.r.t. E_z, which can be found to be given by

$$g^{[n]} = -2 \left(\frac{\overline{\eta} r^{[n-1]}}{\left\| \frac{4}{\mathrm{j}\mu_0} \partial^- B_1^+ \right\|^2} + \frac{\frac{1}{\omega} \partial^- \rho^{[n-1]}}{\left\| B_1^+ \right\|^2} \right), \tag{A3}$$

where the overbar denotes conjugation, $r = \frac{4}{\mathrm{j}\mu_0} \partial^- B_1^+ - \eta E_z$ and $\rho = B_1^+ - \frac{1}{\omega} \partial^+ E_z$. On the update directions we apply an automatic direction reset, by setting negative values to zero. Finally, the step length is obtained by setting the gradient of the functional from Equation (7) w.r.t. α to zero and can be found to be given by

$$\alpha^{[n]} = -\frac{1}{2} \frac{\mathrm{Re}\left\langle g^{[n]}, v^{[n]} \right\rangle}{\dfrac{\left\| \eta v^{[n]} \right\|^2}{\left\| \frac{4}{\mathrm{j}\mu_0} \partial^- B_1^+ \right\|^2} + \dfrac{\left\| \frac{1}{\omega} \partial^+ v^{[n]} \right\|^2}{\left\| B_1^+ \right\|^2}}. \tag{A4}$$

APPENDIX B. DISCRETIZATION

We simplify our notation and set

$$u = E_z, \quad b = B_1^+, \quad \tilde{b} = \frac{4}{\mathrm{j}\mu_0} \partial^- B_1^+, \quad \text{and} \quad \mathcal{D}_e = \frac{1}{\omega} \partial^+, \tag{B1}$$

such that we can write our fundamental equations as

$$\eta u = \tilde{b} \quad \text{and} \quad \mathcal{D}_e u = b. \tag{B2}$$

To discretize both equations of Equation (B2), we first introduce a computational grid consisting of M pixels in the x-direction and N pixels in the y-direction. The side lengths of the pixels in the x- and y-directions are $\delta_x > 0$ and $\delta_y > 0$, respectively, and the midpoints of the pixels have x- and y-coordinates given

$$x_i = \frac{\delta_x}{2} + (i-1)\,\delta_x \quad \text{and} \quad y_j = \frac{\delta_y}{2} + (j-1)\,\delta_y, \tag{B3}$$

for $i = 1, 2, \ldots, M$ and $j = 1, 2, \ldots, N$ with $M\delta_x = \ell_x$ and $N\delta_y = \ell_y$, where $\ell_x > 0$ and $\ell_y > 0$ are the side lengths of the computational domain in the x- and y-direction.

We assume that B_1^+ data is available at the midpoints of the pixels in the computational domain. In other words, the M-by-N matrix

$$\mathsf{B}_1^+ = \begin{pmatrix} B_1^+(x_1, y_1) & B_1^+(x_1, y_2) & \ldots & B_1^+(x_1, y_N) \\ B_1^+(x_2, y_1) & B_1^+(x_2, y_2) & \ldots & B_1^+(x_2, y_N) \\ \vdots & \vdots & \ddots & \vdots \\ B_1^+(x_M, y_1) & B_1^+(x_M, y_2) & \ldots & B_1^+(x_M, y_N) \end{pmatrix} \tag{B4}$$

is known through measurements. We turn this matrix into a vector by applying the vec-operator to matrix B_1^+. The vec-operator stacks the columns of the matrix it operates on from left to right. Applying this operator to matrix B_1^+ produces the MN-by-1 B_1^+ data vector

$$\mathsf{b} = \operatorname{vec}\left(\mathsf{B}_1^+\right). \tag{B5}$$

Subsequently, we construct the discretized counterpart of the scaled and differentiated data $\tilde{b}$. At the midpoints of the pixels, we have

$$\tilde{b}(x_i, y_j) = \frac{4}{\mathrm{j}\mu_0}\,\overline{\partial} B_1^+\big|_{(x_i,y_j)} = \frac{4}{\mathrm{j}\mu_0} \cdot \frac{1}{2}\left(\partial_x B_1^+\big|_{(x_i,y_j)} - \mathrm{j}\,\partial_y B_1^+\big|_{(x_i,y_j)}\right)$$

For interior pixels, the spatial derivative with respect to the x-coordinate is approximated by a central finite-difference formulate, that is, we approximate,

$$\partial_x B_1^+\big|_{(x_i,y_j)} \approx \frac{B_1^+(x_{i+1}, y_j) - B_1^+(x_{i-1}, y_j)}{2\delta_x}$$

for $i = 2, 3, \ldots, M-1$ and $j = 1, 2, \ldots, N$. For boundary pixels, we approximate the derivative by a forward and backward finite-difference formula. Explicitly, for $i = 1$ we use the forward formula

$$\partial_x B_1^+\big|_{(x_1,y_j)} \approx \frac{B_1^+(x_2, y_j) - B_1^+(x_1, y_j)}{\delta_x}$$

for $j = 1, 2, \ldots, N$, while for $i = M$ we use the backward formula

$$\partial_x B_1^+\big|_{(x_M,y_j)} \approx \frac{B_1^+(x_M, y_j) - B_1^+(x_{M-1}, y_j)}{\delta_x}$$

for $j = 1, 2, \ldots, M$. Similar formulas are used to approximate the partial derivative with respect to the y-coordinate.

Replacing the partial derivatives by their finite-difference approximants, we arrive at a finite-difference representation of $\tilde{b}$. The finite-difference formulas can be written in global matrix form through the introduction of the differentiation matrices

$$\mathsf{X} = \frac{1}{2\delta_x}\begin{pmatrix} -2 & 2 & & & & \\ -1 & 0 & 1 & & & \\ & -1 & 0 & 1 & & \\ & & \ddots & \ddots & \ddots & \\ & & & -1 & 0 & 1 \\ & & & & -2 & 2 \end{pmatrix}$$

and

$$\mathsf{Y} = \frac{1}{2\delta_y}\begin{pmatrix} -2 & 2 & & & & \\ -1 & 0 & 1 & & & \\ & -1 & 0 & 1 & & \\ & & \ddots & \ddots & \ddots & \\ & & & -1 & 0 & 1 \\ & & & & -2 & 2 \end{pmatrix}.$$

Note that both matrices are square — matrix X is of order M, while matrix Y is of order N. Finally, introducing the M-by-N matrix

$$\tilde{\mathsf{B}} = \begin{pmatrix} \tilde{b}(x_1, y_1) & \tilde{b}(x_1, y_2) & \dots & \tilde{b}(x_1, y_N) \\ \tilde{b}(x_2, y_1) & \tilde{b}(x_2, y_2) & \dots & \tilde{b}(x_2, y_N) \\ \vdots & \vdots & \ddots & \vdots \\ \tilde{b}(x_M, y_1) & \tilde{b}(x_M, y_2) & \dots & \tilde{b}(x_M, y_N) \end{pmatrix}$$

we can write all finite-difference equations in one single matrix equation as

$$\tilde{\mathsf{B}} = \frac{4}{\mathrm{j}\mu_0} \cdot \frac{1}{2}\left(\mathsf{X}\mathsf{B}_1^{+} - \mathrm{j}\mathsf{B}_1^{+}\mathsf{Y}^{\mathrm{T}}\right).$$

Applying the vec-operator to this equation, using its linearity, and the property

$$\mathrm{vec}\left(\mathsf{AXB}\right) = \left(\mathsf{B}^{\mathrm{T}} \otimes \mathsf{A}\right)\mathrm{vec}\left(\mathsf{X}\right),$$

where $\otimes$ denotes the Kronecker or tensor product, we arrive

$$\tilde{\mathsf{b}} = \mathrm{vec}\left(\tilde{\mathsf{B}}\right) = \frac{4}{\mathrm{j}\mu_0}\,\overline{\mathsf{D}}\mathsf{b},$$

where we have introduced the discretized del-bar operator as

$$\mathsf{D} = \frac{1}{2}\left[\left(\mathsf{I}_N \otimes \mathsf{X}\right) + \mathrm{j}\left(\mathsf{Y} \otimes \mathsf{I}_M\right)\right] \tag{B6}$$

and the overbar denotes complex conjugation. Furthermore, I_M is the identity operator of order M.

Finally, we introduce the field and conductance per unit length matrices as

$$\mathsf{F} = \begin{pmatrix} u(x_1, y_1) & u(x_1, y_2) & \dots & u(x_1, y_N) \\ u(x_2, y_1) & u(x_2, y_2) & \dots & u(x_2, y_N) \\ \vdots & \vdots & \ddots & \vdots \\ u(x_M, y_1) & u(x_M, y_2) & \dots & u(x_M, y_N) \end{pmatrix}$$

and

$$\mathsf{T} = \begin{pmatrix} \eta(x_1, y_1) & \eta(x_1, y_2) & \dots & \eta(x_1, y_N) \\ \eta(x_2, y_1) & \eta(x_2, y_2) & \dots & \eta(x_2, y_N) \\ \vdots & \vdots & \ddots & \vdots \\ \eta(x_M, y_1) & \eta(x_M, y_2) & \dots & \eta(x_M, y_N) \end{pmatrix},$$

respectively. These matrices are turned into vectors as well by once again applying the vec-operator to these equations. We obtain

$$\mathsf{c} = \mathrm{vec}\left(\mathsf{T}\right) \quad \text{and} \quad \mathsf{u} = \mathrm{vec}\left(\mathsf{F}\right).$$

The global discretized field equations are now given by

$$\mathsf{C}\mathsf{u} = \tilde{\mathsf{b}} \quad \text{and} \quad \mathsf{D}_e\mathsf{u} = \mathsf{b},$$

with $\mathsf{C} = \mathrm{diag}(\mathsf{c})$, $\tilde{\mathsf{b}} = -4\mathrm{j}\mu_0^{-1}\overline{\mathsf{D}}\mathsf{b}$, $\mathsf{D}_e = \omega^{-1}\mathsf{D}$, and D is the discretized counterpart of the del operator and is given by Equation (B6).

SUPPLEMENTARY INFORMATION

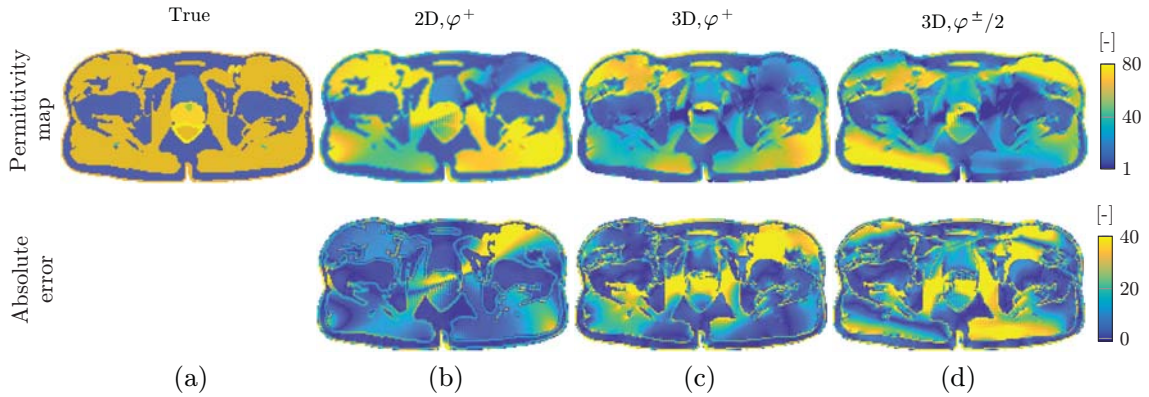

Figure S1. Reconstructed permittivity map (top row) and the corresponding absolute error map (bottom row) of the Duke pelvis model for different B_1^+ datasets.

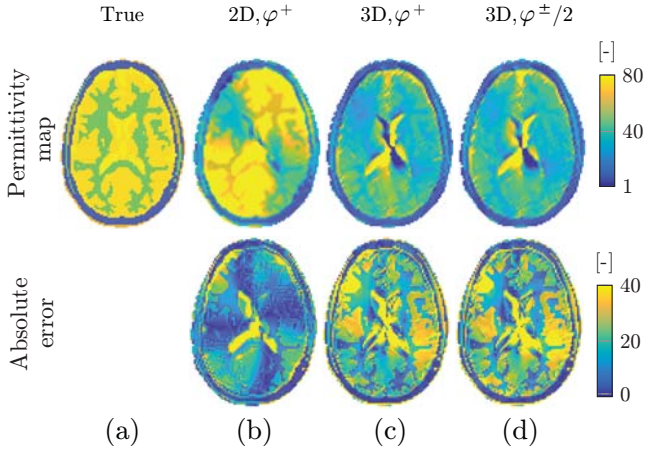

Figure S2. Reconstructed permittivity map (top row) and the corresponding absolute error map (bottom row) of the Ella head model for different transmit field datasets.

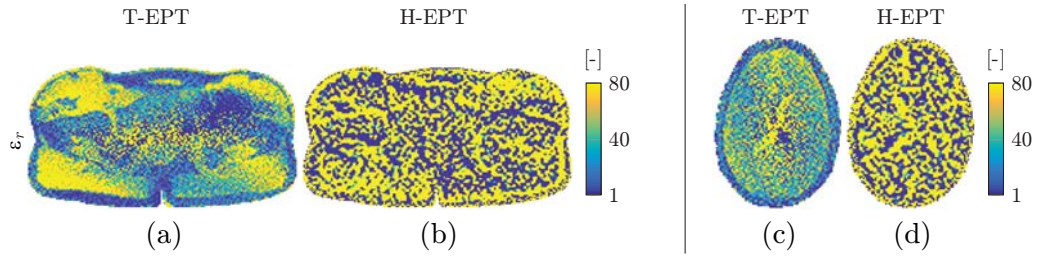

Figure S3. Reconstructed permittivity map of (a), (b) the Duke pelvis model and (c), (d) the Ella head model from noisy three-dimensional transmit field data with an SNR of 100 and with TPA applied.

REFERENCES

1. Balidemaj, E., H. P. Kok, G. Schooneveldt, A. L. van Lier, R. F. Remis, L. J. Stalpers, H. Westerveld, A. J. Nederveen, C. A. van den Berg, and J. Crezee, "Hyperthermia treatment planning for cervical cancer patients based on electrical conductivity tissue properties acquired in vivo with EPT at 3 T MRI," *Int. J. Hyperther.*, Vol. 32, No. 5, 558–568, 2016.

2. Gandhi, O. P. and X. B. Chen, "Specific absorption rates and induced current densities for an anatomy-based model of the human for exposure to time-varying magnetic fields of MRI," *Magn. Reson. Med.*, Vol. 41, No. 1, 816–823, 1999.
3. Kim, S. Y., J. Shin, D. H. Kim, M. J. Kim, E. K. Kim, H. J. Moon, and J. H. Yoon, "Correlation between conductivity and prognostic factors in invasive breast cancer using magnetic resonance electric properties tomography (MREPT)," *Eur. Radiol.*, Vol. 26, No. 7, 2317–2326, 2016.
4. Tha, K. K., U. Katscher, S. Yamaguchi, C. Stehning, S. Terasaka, N. Fujima, K. Kudo, T. Yamamoto, M. van Cauteren, and H. Shirato, "Noninvasive electrical conductivity measurement by MRI: A test of its validity and the electrical conductivity characteristics of glioma," *Eur. Radiol.*, Vol. 28, No. 1, 348–355, 2018.
5. Katscher, U. and C. A. T. van den Berg, "Electric properties tomography: Biochemical, physical and technical background, evaluation and clinical applications," *NMR Biomed.*, Vol. 30, No. 8, e3729, 2017.
6. Liu, J., U. Katscher, and B. He, "Electrical properties tomography based on B_1 maps in MRI: Principles, applications, and challenges," *IEEE Trans. Biomed. Eng.*, Vol. 64, No. 11, 2515–2530, 2017.
7. Leijsen, R., W. Brink, C. van den Berg, A. Webb, and R. Remis, "Electrical properties tomography: A methodological review," *Diagnostics*, Vol. 11, No. 2, 176, 2021.
8. van den Bergen, B., C. C. Stolk, J. B. van den Berg, J. J. Lagendijk, and C. A. van den Berg, "Ultra fast electromagnetic field computations for RF multi-transmit techniques in high field MRI," *Phys. Med. Biol.*, Vol. 54, No. 5, 1253–1264, 2009.
9. Balidemaj, E., C. A. van den Berg, J. Trinks, A. L. van Lier, A. J. Nederveen, L. J. Stalpers, J. A. Lukas, H. Crezee, and R. F. Remis, "CSI-EPT: A contrast source inversion approach for improved MRI-based electric properties tomography," *IEEE Trans. Med. Imag.*, Vol. 34, No. 9, 1788–1796, 2015.
10. Fuchs, P. S., S. Mandija, P. R. Stijnman, W. M. Brink, C. A. van den Berg, and R. F. Remis, "First-order induced current density imaging and electrical properties tomography in MRI," *IEEE T. Comp. Imag.*, Vol. 4, No. 4, 624–631, 2018.
11. Haacke, E. M., L. S. Petropoulos, E. W. Nilges, and D. H. Wu, "Extraction of conductivity and permittivity using magnetic resonance imaging," *Phys. Med. Biol.*, Vol. 36, No. 6, 723–734, 1991.
12. Voigt, T., U. Katscher, and O. Doessel, "Quantitative conductivity and permittivity imaging of the human brain using electric properties tomography," *Magn. Reson. Med.*, Vol. 66, No. 2, 456–466, 2011.
13. Marques, J. P., D. K. Sodickson, O. Ipek, C. M. Collins, and R. Gruetter, "Single acquisition electrical property mapping based on relative coil sensitivities: A proof-of-concept demonstration," *Magn. Reson. Med.*, Vol. 74, No. 1, 185–195, 2015.
14. Hampe, N., M. Herrmann, T. Amthor, C. Findeklee, M. Doneva, and U. Katscher, "Dictionary-based electric properties tomography," *Magn. Reson. Med.*, Vol. 81, No. 1, 342–349, 2019.
15. Mandija, S., E. F. Meliadò, N. R. Huttinga, P. R. Luijten, and C. A. van den Berg, "Opening a new window on MR-based electrical properties tomography with deep learning," *Sci. Rep.*, Vol. 9, No. 1, 1–9, 2019.
16. Hong, R., S. Li, J. Zhang, Y. Zhang, N. Liu, Z. Yu, and Q. H. Liu, "3-D MRI-based electrical properties tomography using the volume integral equation method," *IEEE Trans. Microw. Theory Tech.*, Vol. 65, No. 12, 4802–4811, 2017.
17. Leijsen, R. L., W. M. Brink, C. A. van den Berg, A. G. Webb, and R. F. Remis, "3-D contrast source inversion-electrical properties tomography," *IEEE Trans. Med. Imag.*, Vol. 37, No. 9, 2080–2089, 2018.
18. Serrallés, J. E. C., I. I. Giannakopoulos, B. Zhang, C. Ianniello, M. A. Cloos, A. G. Polimeridis, J. K. White, D. K. Sodickson, L. Daniel, and R. Lattanzi, "Noninvasive estimation of electrical properties from magnetic resonance measurements via global Maxwell tomography and match regularization," *IEEE Trans. Biomed. Eng.*, Vol. 67, No. 1, 3–15, 2019.

19. Van Lier, A. L., D. O. Brunner, K. P. Pruessmann, D. W. Klomp, P. R. Luijten, J. J. Lagendijk, and C. A. van den Berg, "B1+ phase mapping at 7 T and its application for in vivo electrical conductivity mapping," *Magn. Reson. Med.*, Vol. 67, No. 2, 552–561, 2012.
20. Christ, A., et al., "The Virtual Family — Development of surface-based anatomical models of two adults and two children for dosimetric simulations," *Phys. Med. Biol.*, Vol. 55, No. 2, N23–N38, 2009.
21. Mandija, S., A. Sbrizzi, U. Katscher, P. R. Luijten, and C. A. van den Berg, "Error analysis of helmholtz-based MR-electrical properties tomography," *Magn. Reson. Med.*, Vol. 80, No. 1, 90–100, 2018.
22. Lee, S., S. Bulumulla, F. Wiesinger, L. Sacolick, W. Sun, and I. Hancu, "Tissue electrical property mapping from zero echo-time magnetic resonance imaging," *IEEE Trans. Med. Imag.*, Vol. 34, No. 2, 554–550, 2014.
23. Guo, L., J. Jin, M. Li, Y. Wang, C. Liu, F. Liu, and S. Crozier, "Reference-based integral MR-EPT: Simulation and experiment studies at 9.4 T MRI," *IEEE Trans. Biomed. Eng.*, Vol. 66, No. 7, 1832–1843, 2018.
24. Hafalir, F. S., O. F. Oran, N. Gurler, and Y. Z. Ider, "Convection-reaction equation based magnetic resonance electrical properties tomography (cr-MREPT)," *IEEE Trans. Med. Imag.*, Vol. 33, No. 2, 777–793, 2014.
25. Vernickel, P., P. Röschmann, C. Findeklee, K. M. Lüdeke, C. Leussler, J. Overweg, U. Katscher, I. Grässlin, and K. Schünemann, "Eight-channel transmit/receive body MRI coil at 3 T," *Magn. Reson. Med.*, Vol. 58, No. 2, 381–389, 2007.
26. Vaughan, J. T., H. P. Hetherington, J. O. Otu, J. W. Pan, and G. M. Pohost, "High frequency volume coils for clinical NMR imaging and spectroscopy," *Magn. Reson. Med.*, Vol. 32, No. 2, 206–218, 1994.
27. Arduino, A., O. Bottauscio, M. Chiampi, and L. Zilberti, "Magnetic resonance-based imaging of human electric properties with phaseless contrast source inversion," *Inverse Probl.*, Vol. 34, No. 8, 084002, 2018.
28. Gurler, N. and Y. Z. Ider, "Gradient-based electrical conductivity imaging using MR phase," *Magn. Reson. Med.*, Vol. 77, No. 1, 137–150, 2017.
29. Liu, J., X. Zhang, S. Schmitter, P. F. van de Moortele, and B. He, "Gradient-based electrical properties tomography (g EPT): A robust method for mapping electrical properties of biological tissues in vivo using magnetic resonance imaging," *Magn. Reson. Med.*, Vol. 74, No. 3, 634–646, 2015.